Earth and Planetary Science Letters 473 (2017) 215–226

Contents lists available at ScienceDirect

Earth and Planetary Science Letters

www.elsevier.com/locate/epsl

Nucleosynthetic molybdenum isotope anomalies in iron meteorites – new evidence for thermal processing of solar nebula material

Graeme M. Poole [a,b,*], Mark Rehkämper [a,c,**], Barry J. Coles [a], Tatiana Goldberg [a,d], Caroline L. Smith [c]

[a] Department of Earth Science and Engineering, Imperial College London, London SW7 2AZ, UK
[b] School of Earth Sciences, University of Bristol, Bristol BS8 1RJ, UK
[c] Department of Earth Sciences, The Natural History Museum, London SW7 5BD, UK
[d] Institute of Applied Geosciences, TNO, Utrecht, The Netherlands

ARTICLE INFO

Article history:
Received 18 October 2016
Received in revised form 28 March 2017
Accepted 1 May 2017
Available online 20 June 2017
Editor: C. Sotin

Keywords:
nucleosynthetic isotope anomalies
molybdenum
solar nebula
iron meteorites
solar system

ABSTRACT

We have investigated nucleosynthetic Mo isotope anomalies in 38 different bulk iron meteorites from 11 groups, to produce by far the largest and most precise dataset available to date for such samples. All magmatic iron groups were found to display deficits in s-process Mo isotopes, with essentially constant anomalies within but significant variations between groups. Only meteorites of the non-magmatic IAB/IIICD complex revealed terrestrial Mo isotopic compositions.

The improved analytical precision achieved in this study enables two isotopically distinct suites of iron meteorites to be identified. Of these, the *r=p suite* encompasses the IC, IIAB, IIE, IIIAB, IIIE and IVA groups and exhibits relatively modest but 'pure' s-process deficits, relative to Earth. The second *r>p suite* includes groups IIC, IIIF and IVB. These iron meteorites show larger s-process deficits than the *r=p suite*, coupled with an excess of r-process relative to p-process components.

Comparison of the results with data for other elements (e.g., Cr, Ni, Ru, Ti, Zr) suggests that the Mo isotope variability is most likely produced by thermal processing and selective destruction of unstable presolar phases. An updated model is proposed, which relates the iron meteorite suites to different extents of thermal processing in the solar nebula, as governed by heliocentric distance. In detail, the *r=p suite* of iron meteorite parent bodies is inferred to have formed closer to the Sun, where the extent of thermal processing was similar to that experienced by terrestrial material, so that the meteorites exhibit only small s-process deficits relative to Earth. In contrast, the *r>p suite* formed at greater heliocentric distance, where more subtle thermal processing removed a smaller proportion of r- and p-process host phases, thereby generating larger s-process deficits relative to the terrestrial composition. In addition, the thermal conditions enabled selective destruction of p- versus r-isotope carrier phases, to produce the observed divergence of r- and p-process Mo isotope abundances.

1. Introduction

The solar system formed from the collapse of a molecular cloud of interstellar dust and gas featuring isotopically diverse material produced by nuclear reactions in various pre-existing stellar sources. Whilst presolar grains in primitive meteorites show this cloud was isotopically heterogeneous at the grain-size level (Zinner, 2007), it was initially thought planetary bodies evolved from a hot solar nebula that was well-mixed on larger scales. Various more recent studies, however, identified isotopic variations in bulk meteorites for a number of refractory elements, which are interpreted to reflect planetary-scale heterogeneities in presolar matter that place critical constraints on the physical conditions within the solar nebula. The isotopic heterogeneities found for elements including Ba, Ca, Cr, Mo, Nd, Ni, Ru, Ti and Zr thereby stand in contrast to the isotopic homogeneity exhibited by other refractory elements such as Hf and Os (see Dauphas and Schauble, 2016 and Yokoyama and Walker, 2016 for a thorough overview).

Molybdenum is ideally suited as a tracer of planetary-scale isotopic heterogeneity because it has seven isotopes that were produced by distinct nucleosynthetic processes. The s-process contri-

* Corresponding author at: School of Earth Sciences, University of Bristol, Bristol BS8 1RJ, UK.
** Corresponding author at: Department of Earth Science and Engineering, Imperial College London, London SW7 2AZ, UK.
E-mail addresses: graeme.poole@bristol.ac.uk (G.M. Poole), markrehk@imperial.ac.uk (M. Rehkämper).

http://dx.doi.org/10.1016/j.epsl.2017.05.001

butions to ^{94}Mo, ^{95}Mo, ^{96}Mo, ^{97}Mo, ^{98}Mo and ^{100}Mo are thought to be from the main s-process in asymptotic giant branch (AGB) stars, while the r-process contributions to the neutron-rich isotopes (^{95}Mo, ^{97}Mo, ^{98}Mo and ^{100}Mo) are argued to be produced by the weak r-process and charged particle reactions (CPRs) in Type II supernovae, with contributions from the main r-process (e.g., Qian and Wasserburg, 2007). Traditionally, models of p-process nucleosynthesis were unable to reproduce the measured abundances of ^{92}Mo and ^{94}Mo, but more recent studies have rectified this problem. In detail, it was proposed that CPRs in the neutrino-driven winds of Type II and photodisintegration reactions (γ-process) in Type Ia supernovae can account for the observed ^{92}Mo and ^{94}Mo abundances (e.g., Travaglio et al., 2015; Wanajo et al., 2011), though this is contested by other workers (e.g., Fisker et al., 2009).

The existence of planetary-scale nucleosynthetic Mo isotope anomalies was first established by the bulk meteorite analyses of Dauphas et al. (2002). A similar but more recent investigation (Burkhardt et al., 2011) used improved methods to produce a comprehensive Mo isotope dataset for a wider range of meteorite types, with a precision several times better than that reported in earlier studies. The latter study found that all chondrites and iron meteorites (except for the non-magmatic IAB/IIICD group), as well as two pallasites, exhibited clear s-process deficits. In contrast, analyses of Martian meteorites and an angrite revealed terrestrial Mo isotope compositions. The authors were therefore able to conclude that Earth, Mars, and the parent bodies of angrites and non-magmatic IAB/IIICD irons accreted from material with a higher proportion of s-process Mo isotopes than the chondrite, pallasite and other iron meteorite parent bodies.

Given the abundance of available data, any model that is proposed to account for the observed nucleosynthetic Mo isotope anomalies should also be able to explain the isotopic heterogeneity or homogeneity found for other refractory elements. A number of such scenarios have been posited, including inefficient/incomplete mixing in the solar nebula (e.g., Schiller et al., 2015), late injection (e.g., Qin et al., 2011), grain size sorting (Dauphas et al., 2010), thermal processing (e.g., Burkhardt et al., 2012b), and parent body processes (e.g., aqueous alteration – Yokoyama et al., 2011). To further elucidate the validity of these concepts, we have obtained precise Mo isotope data for 11 groups of iron meteorites. With better precision than previous studies, the results provide new constraints on planetary-scale processes in the solar nebula and help resolve the origin of nebula-wide nucleosynthetic isotope anomalies.

2. Analytical techniques

Only a brief outline of the methods is presented here, with further details available in the Supplementary Material. Fifty-three specimens from 38 distinct iron meteorites of 11 different groups were obtained from the Natural History Museum, London, and private collectors. Separation of Mo was achieved by a two-stage procedure, which applies anion exchange chromatography with Bio-Rad AG1-X8 resin. Following the chemistry, the purified Mo fractions typically had Ru/Mo and Zr/Mo ratios of lower than 3×10^{-5} and 4×10^{-5}, respectively, corresponding to corrections on Mo isotope ratios of less than 50 ppm for Ru interferences, and of less than 100 ppm for Zr.

Isotope measurements were performed with a Nu Plasma HR MC-ICP-MS, in a two-sequence routine. A simultaneous measurement of ^{92}Mo, ^{94}Mo, ^{95}Mo, ^{96}Mo, ^{97}Mo, ^{98}Mo, ^{100}Mo and ^{99}Ru ion beams was performed in the first sequence, while the second sequence, which immediately followed the first, collected the ^{90}Zr/^{95}Mo ratio for Zr interference corrections. Typical sensitivity for Mo was 150–180 V/ppm.

Instrumental mass bias was corrected by internal normalisation to ^{98}Mo/^{96}Mo = 1.453174 ('8/6'), ^{92}Mo/^{98}Mo = 0.607898 ('2/8') and ^{97}Mo/^{95}Mo = 0.602083 ('7/5'), using the exponential law (Lu and Masuda, 1994). All sample data are given relative to the mean of several (typically $n = 4$) bracketing runs of NIST SRM 3134 Mo made up to closely match the Mo concentration of the samples (~200 ppb), and reported in ε^iMo notation (Equation (1)), where ^{9y}Mo/^{9x}Mo is the normalising ratio:

$$\varepsilon^i \mathrm{Mo}_{(y/x)} = \left[(^i\mathrm{Mo}/^{9x}\mathrm{Mo})_{\mathrm{sample}} / (^i\mathrm{Mo}/^{9x}\mathrm{Mo})_{\mathrm{standard}} - 1 \right] \times 10^4 \quad (1)$$

Typical external reproducibility (2σ = 2sd) of the standard measurements over a single session ($n > 50$) ranged from ±0.47 for $\varepsilon^{92}\mathrm{Mo}_{(8/6)}$ to ±0.15 for $\varepsilon^{96}\mathrm{Mo}_{(2/8)}$, while internal precision (2se) ranged from ±0.29 to ±0.09 ($\varepsilon^{92}\mathrm{Mo}_{(8/6)}$ and $\varepsilon^{96}\mathrm{Mo}_{(2/8)}$, respectively). The precision achieved here is generally a factor of ~1.5 better than reported in the most precise previous study by Burkhardt et al. (2011). Most likely, the improved precision arises from the higher ion beam intensities that were obtained here for analyses of ~200 ppb Mo solutions, whilst Burkhardt et al. (2011) utilised ~100 ppb Mo solutions.

The robustness and reproducibility of the Mo separation procedure and MC-ICP-MS Mo isotope measurements were repeatedly evaluated by analyses of terrestrial standard reference materials, which yielded the expected Mo isotope compositions throughout (see Supplementary Material).

3. Results

All Mo isotope results for normalisation to ^{98}Mo/^{96}Mo and ^{97}Mo/^{95}Mo are summarised in Fig. 1, with corresponding data presented in Table 1 and Table 2. Also shown in Fig. 1 are the expected effects of increasing and decreasing the proportions of p-, s- and r-process components on the Mo isotope patterns. Details of this modelling, as well as the results using normalisation to ^{92}Mo/^{98}Mo, are outlined in the Supplementary Material.

For all normalising schemes, meteorites of all groups (except IAB/IIICD) exhibit offsets from $\varepsilon^i\mathrm{Mo} = 0$. The results agree most with the corresponding models of s-process deficits (solid green lines, Fig. 1c–d). For instance, in the data normalised to ^{98}Mo/^{96}Mo (Fig. 1a), the magnitude of anomalies decreases in the order $\varepsilon^{92}\mathrm{Mo}_{(8/6)} > \varepsilon^{94}\mathrm{Mo}_{(8/6)} > \varepsilon^{95}\mathrm{Mo}_{(8/6)} > \varepsilon^{100}\mathrm{Mo}_{(8/6)} > \varepsilon^{97}\mathrm{Mo}_{(8/6)}$, giving rise to the characteristic w-shaped pattern of s-process deficits, as depicted by the solid green line in Fig. 1c.

Meteorites from the same group display identical or nearly identical Mo isotopic anomalies (within uncertainty), such that the Mo isotope composition of any meteorite can be considered as representative of the complete metal core of its parent body. Yet, the extent of the anomalies displayed by the different magmatic iron groups is variable. The IIC irons display by far the most extreme isotope compositions with $\varepsilon^{92}\mathrm{Mo}_{(8/6)} = +3.12 \pm 0.27$, while the IVAs are the least anomalous of the magmatic iron groups ($\varepsilon^{92}\mathrm{Mo}_{(8/6)} = +0.95 \pm 0.19$). The non-magmatic IAB and IIICD groups, often termed the IAB/IIICD complex (e.g., Wasson and Kallemeyn, 2002), present Mo isotope compositions indistinguishable from terrestrial Mo, while the non-magmatic IIE group is slightly anomalous with $\varepsilon^{92}\mathrm{Mo}_{(8/6)} = +0.86 \pm 0.32$.

4. Discussion

4.1. Comparison to literature

While the results presented here are more abundant and precise than the data of Burkhardt et al. (2011) for irons, excellent agreement is observed between these two investigations. Principally, Burkhardt et al. (2011) also found that iron meteorite

Table 1
Molybdenum isotope compositions of iron meteorites, normalised to $^{98}Mo/^{96}Mo$.

Group	Sample	N[a]	$\varepsilon^{92}Mo_{(8/6)}$[b]	$\varepsilon^{94}Mo_{(8/6)}$[b]	$\varepsilon^{95}Mo_{(8/6)}$[b]	$\varepsilon^{97}Mo_{(8/6)}$[b]	$\varepsilon^{100}Mo_{(8/6)}$[b]
IAB	Bitburg	10	−0.10 ± 0.07	−0.01 ± 0.05	−0.01 ± 0.05	−0.05 ± 0.03	0.00 ± 0.06
	Campo del Cielo 1	11	0.32 ± 0.11	0.22 ± 0.04	−0.05 ± 0.05	−0.05 ± 0.05	0.06 ± 0.08
	Campo del Cielo 2	9	0.13 ± 0.13	0.15 ± 0.04	0.01 ± 0.06	−0.04 ± 0.02	−0.04 ± 0.07
	Campo del Cielo 3	9	0.10 ± 0.09	0.05 ± 0.06	−0.11 ± 0.09	0.03 ± 0.06	0.05 ± 0.11
	Canyon Diablo 1	6	−0.06 ± 0.23	−0.01 ± 0.09	−0.14 ± 0.03	−0.04 ± 0.08	0.24 ± 0.18
	Canyon Diablo 2	6	−0.11 ± 0.24	−0.05 ± 0.07	−0.19 ± 0.06	−0.06 ± 0.06	0.10 ± 0.08
	Cosby's Creek	13	−0.01 ± 0.07	−0.01 ± 0.06	0.02 ± 0.04	−0.06 ± 0.03	−0.08 ± 0.06
	Odessa	10	0.01 ± 0.11	0.05 ± 0.08	−0.16 ± 0.01	0.01 ± 0.06	0.18 ± 0.05
	Toluca	12	0.00 ± 0.08	0.14 ± 0.06	−0.06 ± 0.04	−0.05 ± 0.03	0.02 ± 0.06
	IAB MEAN		**0.00 ± 0.08**	**0.05 ± 0.06**	**−0.07 ± 0.06**	**−0.04 ± 0.02**	**0.05 ± 0.08**
IC	Arispe 1	8	1.04 ± 0.10	0.87 ± 0.06	0.25 ± 0.07	0.22 ± 0.08	0.38 ± 0.07
	Arispe 2	7	0.98 ± 0.14	0.85 ± 0.11	0.28 ± 0.06	0.16 ± 0.06	0.24 ± 0.10
	Arispe 3	4	1.20 ± 0.13	0.95 ± 0.18	0.32 ± 0.07	0.21 ± 0.06	0.16 ± 0.07
	Arispe 4	8	1.03 ± 0.13	0.87 ± 0.08	0.31 ± 0.13	0.20 ± 0.05	0.25 ± 0.15
	Bendego 1	9	1.16 ± 0.18	0.94 ± 0.07	0.28 ± 0.06	0.20 ± 0.08	0.35 ± 0.11
	Bendego 2	7	0.93 ± 0.10	0.80 ± 0.08	0.23 ± 0.05	0.12 ± 0.07	0.22 ± 0.08
	Santa Rosa	8	1.14 ± 0.15	0.99 ± 0.08	0.34 ± 0.08	0.18 ± 0.05	0.34 ± 0.03
	IC MEAN		**1.08 ± 0.06**	**0.92 ± 0.08**	**0.30 ± 0.05**	**0.18 ± 0.02**	**0.30 ± 0.05**
IIAB	Coahuila	12	1.48 ± 0.09	1.18 ± 0.06	0.49 ± 0.08	0.27 ± 0.04	0.44 ± 0.06
	Murphy	11	1.26 ± 0.14	1.08 ± 0.10	0.47 ± 0.07	0.25 ± 0.05	0.41 ± 0.08
	Negrillos	10	1.53 ± 0.12	1.23 ± 0.12	0.47 ± 0.05	0.27 ± 0.06	0.25 ± 0.09
	North Chile	16	1.52 ± 0.14	1.25 ± 0.09	0.57 ± 0.06	0.28 ± 0.03	0.47 ± 0.08
	Sikhote Alin 1	13	1.58 ± 0.07	1.23 ± 0.07	0.50 ± 0.05	0.22 ± 0.07	0.42 ± 0.09
	Sikhote Alin 2	8	1.38 ± 0.14	1.18 ± 0.04	0.58 ± 0.09	0.25 ± 0.07	0.26 ± 0.06
	IIAB MEAN		**1.45 ± 0.10**	**1.19 ± 0.06**	**0.51 ± 0.04**	**0.26 ± 0.02**	**0.38 ± 0.08**
IIC	Ballinoo	7	3.07 ± 0.18	2.35 ± 0.15	1.62 ± 0.11	0.81 ± 0.06	1.05 ± 0.12
	Kumerina	10	2.92 ± 0.09	2.28 ± 0.08	1.53 ± 0.07	0.79 ± 0.06	1.12 ± 0.08
	Salt River	6	3.38 ± 0.14	2.56 ± 0.06	1.68 ± 0.10	0.87 ± 0.09	0.84 ± 0.09
	IIC MEAN		**3.12 ± 0.27**	**2.40 ± 0.16**	**1.61 ± 0.09**	**0.82 ± 0.05**	**1.00 ± 0.17**
IIE	Kodaikanal	6	1.04 ± 0.16	0.79 ± 0.06	0.34 ± 0.06	0.10 ± 0.03	0.24 ± 0.12
	Verkhne Dnieprovsk	8	0.99 ± 0.16	0.78 ± 0.10	0.37 ± 0.04	0.19 ± 0.06	0.17 ± 0.08
	Weekeroo Station	5	0.54 ± 0.11	0.57 ± 0.15	0.16 ± 0.05	0.08 ± 0.03	0.29 ± 0.11
	IIE MEAN		**0.86 ± 0.32**	**0.71 ± 0.15**	**0.29 ± 0.13**	**0.12 ± 0.07**	**0.24 ± 0.07**
IIIAB	Bear Creek	10	1.16 ± 0.18	1.00 ± 0.14	0.44 ± 0.08	0.19 ± 0.05	0.41 ± 0.06
	Cape York	8	1.31 ± 0.09	1.09 ± 0.06	0.44 ± 0.07	0.16 ± 0.08	0.36 ± 0.04
	Charcas 1	6	1.10 ± 0.07	0.89 ± 0.08	0.32 ± 0.10	0.12 ± 0.06	0.35 ± 0.16
	Charcas 2	9	1.02 ± 0.13	0.92 ± 0.09	0.30 ± 0.10	0.22 ± 0.03	0.41 ± 0.07
	Henbury 1	6	1.12 ± 0.14	0.97 ± 0.06	0.33 ± 0.07	0.16 ± 0.08	0.29 ± 0.06
	Henbury 2	10	1.20 ± 0.19	1.06 ± 0.09	0.44 ± 0.07	0.22 ± 0.07	0.24 ± 0.05
	Lenarto	10	1.39 ± 0.10	1.13 ± 0.08	0.51 ± 0.05	0.17 ± 0.05	0.30 ± 0.08
	Santa Apolonia 1	6	1.25 ± 0.27	0.99 ± 0.18	0.42 ± 0.10	0.21 ± 0.06	0.33 ± 0.13
	Santa Apolonia 2	8	1.18 ± 0.14	0.95 ± 0.07	0.35 ± 0.05	0.16 ± 0.05	0.33 ± 0.13
	Verkhne Udinsk	7	1.44 ± 0.14	1.11 ± 0.08	0.42 ± 0.08	0.18 ± 0.05	0.49 ± 0.09
	Williamette	8	1.40 ± 0.19	1.06 ± 0.20	0.51 ± 0.11	0.21 ± 0.06	0.34 ± 0.03
	IIIAB MEAN		**1.27 ± 0.10**	**1.04 ± 0.05**	**0.43 ± 0.05**	**0.18 ± 0.01**	**0.36 ± 0.05**
IIICD	Carlton 1	5	0.37 ± 0.18	0.27 ± 0.11	0.02 ± 0.08	−0.02 ± 0.03	0.00 ± 0.09
	Carlton 2	2	0.32 ± 0.20	0.08 ± 0.04	−0.10 ± 0.08	−0.05 ± 0.20	0.08 ± 0.17
	Nantan 1	10	0.14 ± 0.17	0.21 ± 0.13	0.09 ± 0.10	0.02 ± 0.07	0.08 ± 0.07
	Nantan 2	11	−0.03 ± 0.11	0.08 ± 0.11	−0.06 ± 0.08	−0.04 ± 0.05	0.05 ± 0.07
	IIICD MEAN		**0.20 ± 0.29**	**0.16 ± 0.03**	**−0.01 ± 0.06**	**−0.02 ± 0.02**	**0.05 ± 0.03**
IIIE	Staunton	8	1.40 ± 0.19	1.07 ± 0.13	0.45 ± 0.09	0.25 ± 0.07	0.40 ± 0.15
IIIF	Clark County	7	1.70 ± 0.09	1.24 ± 0.05	0.92 ± 0.05	0.39 ± 0.06	0.59 ± 0.04
IVA	Gibeon 1	5	1.11 ± 0.25	0.85 ± 0.25	0.42 ± 0.24	0.18 ± 0.10	0.27 ± 0.18
	Gibeon 2	4	1.02 ± 0.15	0.80 ± 0.19	0.37 ± 0.10	0.20 ± 0.04	0.17 ± 0.19
	Muonionalusta	7	0.76 ± 0.28	0.64 ± 0.14	0.30 ± 0.11	0.20 ± 0.08	0.46 ± 0.04
	Obernkirchen	6	1.01 ± 0.10	0.82 ± 0.05	0.33 ± 0.09	0.17 ± 0.06	0.22 ± 0.09
	IVA MEAN		**0.95 ± 0.19**	**0.76 ± 0.12**	**0.34 ± 0.05**	**0.18 ± 0.02**	**0.30 ± 0.16**
IVB	Cape of Good Hope	10	2.04 ± 0.14	1.38 ± 0.10	0.98 ± 0.06	0.49 ± 0.06	0.72 ± 0.05
	Santa Clara	12	1.93 ± 0.14	1.37 ± 0.10	0.97 ± 0.06	0.51 ± 0.07	0.84 ± 0.09
	Tlacotopec 1	9	1.86 ± 0.17	1.34 ± 0.11	0.84 ± 0.07	0.47 ± 0.05	0.80 ± 0.08
	Tlacotopec 2	12	1.47 ± 0.11	1.14 ± 0.09	0.65 ± 0.06	0.46 ± 0.04	0.92 ± 0.10
	IVB MEAN		**1.88 ± 0.22**	**1.33 ± 0.09**	**0.90 ± 0.15**	**0.49 ± 0.03**	**0.81 ± 0.09**

[a] Number of times sample was analysed;
[b] Normalised to $^{98}Mo/^{96}Mo = 1.453174$ (Lu and Masuda, 1994), using the exponential law, $\varepsilon^{i}Mo = [(^{i}Mo/^{96}Mo)_{smp}/(^{i}Mo/^{96}Mo)_{std} - 1] \times 10^{4}$; Uncertainties for samples are $2se = 2\sigma/\sqrt{n}$, where n is the number of times a sample was analysed. Uncertainties for group means are $2se = 2\sigma/\sqrt{n}$, where n is the number of 'unique' samples analysed for that group (for samples with multiple specimens, the mean of the specimens is taken to represent that sample when calculating the group mean).

Table 2
Molybdenum isotope compositions of iron meteorites, normalised to $^{97}Mo/^{95}Mo$.

Group	Sample	N[a]	$\varepsilon^{92}Mo_{(7/5)}$[b]	$\varepsilon^{94}Mo_{(7/5)}$[b]	$\varepsilon^{96}Mo_{(7/5)}$[b]	$\varepsilon^{98}Mo_{(7/5)}$[b]	$\varepsilon^{100}Mo_{(7/5)}$[b]
IAB	Bitburg	10	−0.08 ± 0.12	−0.04 ± 0.05	0.02 ± 0.03	0.02 ± 0.06	0.04 ± 0.11
	Campo del Cielo 1	11	0.38 ± 0.05	0.23 ± 0.07	0.04 ± 0.05	0.06 ± 0.08	0.14 ± 0.18
	Campo del Cielo 2	9	0.04 ± 0.09	0.14 ± 0.08	0.01 ± 0.04	0.05 ± 0.04	0.09 ± 0.13
	Campo del Cielo 3	9	0.27 ± 0.14	0.19 ± 0.09	0.03 ± 0.06	−0.03 ± 0.12	−0.06 ± 0.18
	Canyon Diablo 1	6	0.30 ± 0.15	0.20 ± 0.10	0.11 ± 0.05	−0.03 ± 0.09	0.10 ± 0.28
	Canyon Diablo 2	6	0.32 ± 0.25	0.24 ± 0.10	0.14 ± 0.04	−0.04 ± 0.08	−0.07 ± 0.15
	Cosby's Creek	13	−0.24 ± 0.10	−0.08 ± 0.04	0.01 ± 0.03	0.10 ± 0.05	0.08 ± 0.13
	Odessa	10	0.43 ± 0.10	0.29 ± 0.06	0.10 ± 0.05	−0.09 ± 0.06	−0.12 ± 0.07
	Toluca	12	0.12 ± 0.06	0.22 ± 0.05	0.06 ± 0.03	0.05 ± 0.05	0.03 ± 0.10
	IAB MEAN		**0.13 ± 0.21**	**0.13 ± 0.12**	**0.06 ± 0.04**	**0.01 ± 0.05**	**0.02 ± 0.06**
IC	Arispe 1	8	0.81 ± 0.10	0.61 ± 0.02	−0.20 ± 0.05	−0.15 ± 0.06	0.18 ± 0.16
	Arispe 2	7	0.54 ± 0.11	0.56 ± 0.09	−0.20 ± 0.03	−0.10 ± 0.06	0.21 ± 0.15
	Arispe 3	4	0.71 ± 0.14	0.49 ± 0.22	−0.24 ± 0.04	−0.15 ± 0.09	0.18 ± 0.18
	Arispe 4	8	0.51 ± 0.20	0.51 ± 0.12	−0.22 ± 0.07	−0.16 ± 0.08	0.23 ± 0.07
	Bendego 1	9	0.62 ± 0.08	0.63 ± 0.03	−0.22 ± 0.05	−0.14 ± 0.10	0.29 ± 0.18
	Bendego 2	7	0.54 ± 0.11	0.51 ± 0.07	−0.17 ± 0.06	−0.06 ± 0.07	0.33 ± 0.12
	Santa Rosa	8	0.51 ± 0.12	0.53 ± 0.09	−0.24 ± 0.07	−0.06 ± 0.05	0.39 ± 0.07
	IC MEAN		**0.58 ± 0.08**	**0.55 ± 0.02**	**−0.21 ± 0.03**	**−0.10 ± 0.05**	**0.30 ± 0.11**
IIAB	Coahuila	12	0.61 ± 0.08	0.56 ± 0.05	−0.37 ± 0.05	−0.14 ± 0.05	0.44 ± 0.10
	Murphy	11	0.47 ± 0.18	0.54 ± 0.07	−0.36 ± 0.04	−0.15 ± 0.08	0.41 ± 0.14
	Negrillos	10	0.44 ± 0.10	0.48 ± 0.05	−0.36 ± 0.04	−0.14 ± 0.05	0.50 ± 0.04
	North Chile	16	0.52 ± 0.12	0.57 ± 0.06	−0.41 ± 0.04	−0.15 ± 0.05	0.57 ± 0.13
	Sikhote Alin 1	13	0.52 ± 0.08	0.60 ± 0.05	−0.35 ± 0.06	−0.09 ± 0.07	0.56 ± 0.10
	Sikhote Alin 2	8	0.34 ± 0.12	0.48 ± 0.03	−0.38 ± 0.05	−0.04 ± 0.12	0.52 ± 0.11
	IIAB MEAN		**0.50 ± 0.07**	**0.54 ± 0.03**	**−0.38 ± 0.02**	**−0.13 ± 0.03**	**0.49 ± 0.06**
IIC	Ballinoo	7	0.30 ± 0.16	0.30 ± 0.06	−1.16 ± 0.06	−0.40 ± 0.10	1.38 ± 0.16
	Kumerina	10	0.36 ± 0.10	0.37 ± 0.07	−1.14 ± 0.05	−0.38 ± 0.07	1.41 ± 0.11
	Salt River	6	0.28 ± 0.19	0.35 ± 0.13	−1.26 ± 0.07	−0.47 ± 0.12	1.19 ± 0.20
	IIC MEAN		**0.31 ± 0.05**	**0.34 ± 0.04**	**−1.19 ± 0.07**	**−0.42 ± 0.05**	**1.33 ± 0.14**
IIE	Kodaikanal	6	0.32 ± 0.14	0.37 ± 0.09	−0.22 ± 0.04	0.01 ± 0.08	0.40 ± 0.10
	Verkhne Dnieprovsk	8	0.29 ± 0.18	0.30 ± 0.07	−0.29 ± 0.04	−0.08 ± 0.09	0.29 ± 0.16
	Weekeroo Station	5	0.24 ± 0.13	0.32 ± 0.10	−0.12 ± 0.04	−0.01 ± 0.07	0.36 ± 0.13
	IIE MEAN		**0.29 ± 0.05**	**0.33 ± 0.04**	**−0.21 ± 0.10**	**−0.02 ± 0.05**	**0.35 ± 0.07**
IIIAB	Bear Creek	10	0.49 ± 0.11	0.51 ± 0.05	−0.29 ± 0.09	−0.10 ± 0.05	0.49 ± 0.05
	Cape York	8	0.48 ± 0.03	0.50 ± 0.05	−0.29 ± 0.06	−0.02 ± 0.09	0.57 ± 0.15
	Charcas 1	6	0.50 ± 0.24	0.54 ± 0.10	−0.19 ± 0.06	−0.02 ± 0.07	0.53 ± 0.16
	Charcas 2	9	0.74 ± 0.05	0.64 ± 0.09	−0.26 ± 0.06	−0.16 ± 0.04	0.28 ± 0.14
	Henbury 1	6	0.52 ± 0.18	0.54 ± 0.04	−0.25 ± 0.06	−0.10 ± 0.10	0.36 ± 0.18
	Henbury 2	10	0.49 ± 0.16	0.55 ± 0.10	−0.31 ± 0.07	−0.11 ± 0.04	0.34 ± 0.09
	Lenarto	10	0.44 ± 0.06	0.51 ± 0.06	−0.35 ± 0.04	−0.06 ± 0.08	0.55 ± 0.19
	Santa Apolonia 1	6	0.44 ± 0.12	0.48 ± 0.11	−0.28 ± 0.08	−0.08 ± 0.07	0.44 ± 0.16
	Santa Apolonia 2	8	0.46 ± 0.13	0.50 ± 0.06	−0.23 ± 0.04	−0.06 ± 0.07	0.48 ± 0.22
	Verkhne Udinsk	7	0.59 ± 0.08	0.54 ± 0.07	−0.30 ± 0.06	−0.07 ± 0.07	0.61 ± 0.14
	Williamette	8	0.39 ± 0.07	0.41 ± 0.10	−0.35 ± 0.08	−0.04 ± 0.05	0.60 ± 0.12
	IIIAB MEAN		**0.50 ± 0.05**	**0.51 ± 0.04**	**−0.29 ± 0.03**	**−0.07 ± 0.02**	**0.51 ± 0.07**
IIICD	Carlton 1	5	0.20 ± 0.18	0.27 ± 0.14	0.03 ± 0.04	0.08 ± 0.07	0.03 ± 0.22
	Carlton 2	2	0.39 ± 0.36	0.19 ± 0.04	0.05 ± 0.05	0.03 ± 0.49	0.05 ± 0.35
	Nantan 1	10	0.16 ± 0.14	0.14 ± 0.03	0.02 ± 0.07	0.04 ± 0.06	0.12 ± 0.12
	Nantan 2	11	0.04 ± 0.08	0.13 ± 0.07	0.06 ± 0.06	0.07 ± 0.06	0.06 ± 0.10
	IIICD MEAN		**0.20 ± 0.20**	**0.18 ± 0.09**	**0.04 ± 0.00**	**0.05 ± 0.00**	**0.07 ± 0.05**
IIIE	Staunton	8	0.61 ± 0.12	0.53 ± 0.03	−0.32 ± 0.06	−0.10 ± 0.06	0.50 ± 0.20
IIIF	Clark County	7	−0.08 ± 0.12	0.02 ± 0.07	−0.65 ± 0.02	−0.14 ± 0.06	0.94 ± 0.11
IVA	Gibeon 1	5	0.30 ± 0.20	0.30 ± 0.10	−0.27 ± 0.15	0.01 ± 0.11	0.50 ± 0.11
	Gibeon 2	4	0.39 ± 0.17	0.36 ± 0.10	−0.25 ± 0.07	−0.04 ± 0.06	0.22 ± 0.05
	Muonionalusta	7	0.28 ± 0.19	0.29 ± 0.09	−0.24 ± 0.09	−0.13 ± 0.09	0.37 ± 0.18
	Obernkirchen	6	0.45 ± 0.19	0.38 ± 0.09	−0.24 ± 0.07	−0.09 ± 0.07	0.30 ± 0.13
	IVA MEAN		**0.36 ± 0.10**	**0.33 ± 0.05**	**−0.25 ± 0.01**	**−0.08 ± 0.07**	**0.34 ± 0.04**
IVB	Cape of Good Hope	10	0.20 ± 0.17	0.15 ± 0.11	−0.74 ± 0.04	−0.26 ± 0.08	0.94 ± 0.20
	Santa Clara	12	0.25 ± 0.08	0.15 ± 0.05	−0.73 ± 0.06	−0.29 ± 0.09	0.99 ± 0.12
	Tlacotopec 1	9	0.38 ± 0.10	0.33 ± 0.07	−0.63 ± 0.05	−0.26 ± 0.06	0.90 ± 0.11
	Tlacotopec 2	12	0.50 ± 0.12	0.37 ± 0.06	−0.57 ± 0.03	−0.32 ± 0.08	0.72 ± 0.09
	IVB MEAN		**0.30 ± 0.15**	**0.21 ± 0.13**	**−0.69 ± 0.09**	**−0.28 ± 0.02**	**0.91 ± 0.11**

[a] Number of times sample was analysed;
[b] Normalised to $^{97}Mo/^{95}Mo = 0.602083$ (Lu and Masuda, 1994), using the exponential law, $\varepsilon^{i}Mo = [(^{i}Mo/^{95}Mo)_{smp}/(^{i}Mo/^{95}Mo)_{std} - 1] \times 10^{4}$; Uncertainties for samples are $2se = 2\sigma/\sqrt{n}$, where n is the number of times a sample was analysed. Uncertainties for group means are $2se = 2\sigma/\sqrt{n}$, where n is the number of 'unique' samples analysed for that group (for samples with multiple specimens, the mean of the specimens is taken to represent that sample when calculating the group mean).

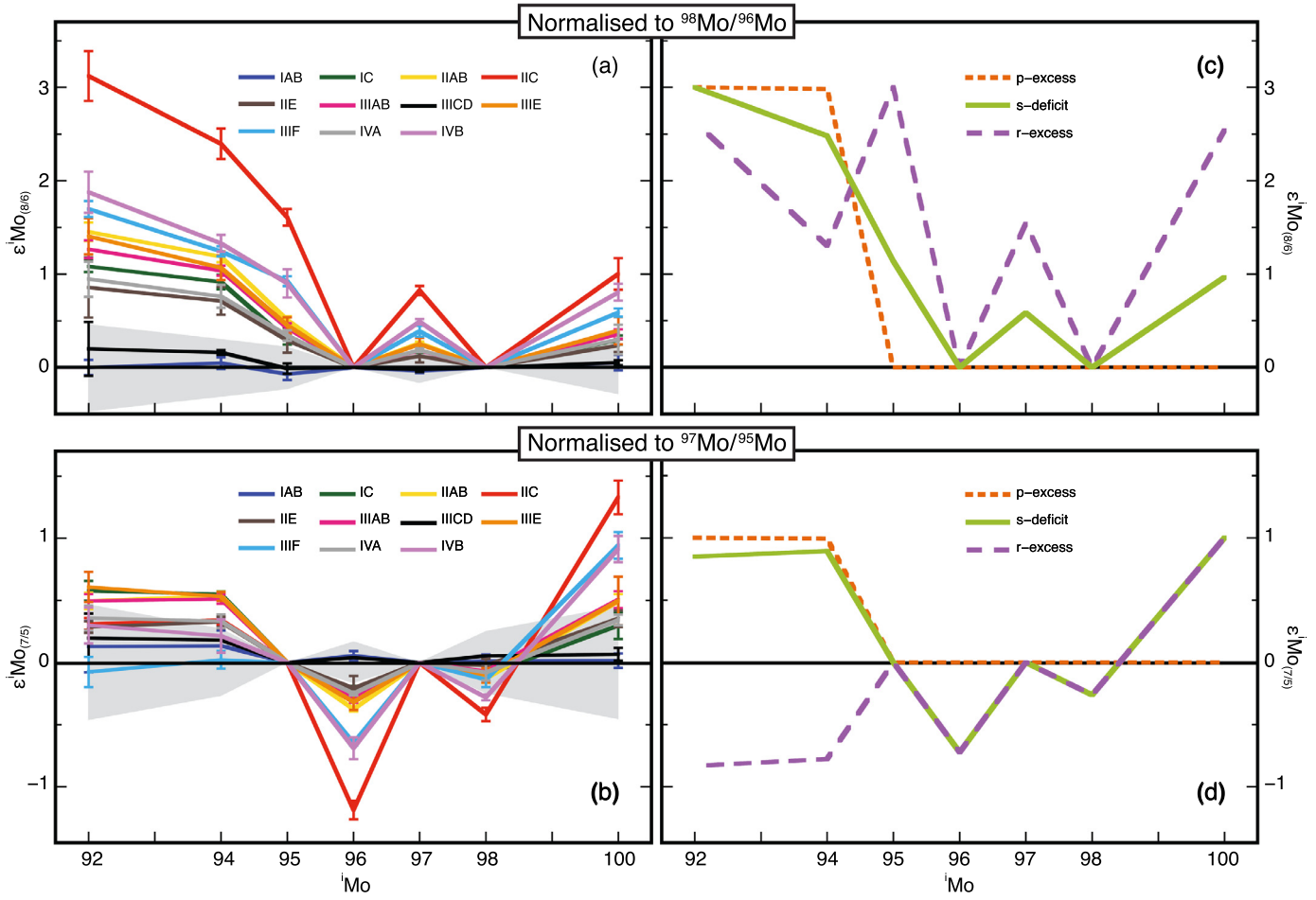

Fig. 1. Molybdenum isotope data for iron meteorites, with modelled effects of variations in p-, s- and r-process components for comparison. Shown in (a) and (b) are group means ±2se, measured relative to NIST SRM 3134. Grey-shaded area represents reproducibility (2σ) of the bracketing SRM runs, which represent the terrestrial Mo isotope composition. Modelled effects in (c) and (d) are calculated by mixing distinct nucleosynthetic components with terrestrial Mo isotope compositions. For consistency, all terrestrial Mo isotope abundances are from the same data set (Lu and Masuda, 1994), as are all nucleosynthetic contributions (Arlandini et al., 1999). For each normalisation, the models are scaled to best match the magnitude of the observed anomalies in the measured results. (For interpretation of the references to colour in this figure, the reader is referred to the web version of this article.)

groups IC, IIAB, IID, IIE, IIIAB, IIIE, IIIF, IVA and IVB possess s-process deficits in the ε-unit range, while the IAB/IIICD group appears to have a terrestrial Mo isotope composition. Intriguingly, our observation that the previously unmeasured IICs are significantly more anomalous than all iron meteorites analysed to date, suggests that it may be fruitful to further explore rare or ungrouped irons.

In addition, the Mo data presented here agree, for the most part, with the results of Dauphas et al. (2002), who also found variable s-deficits in magmatic iron meteorites. Yet, whereas Dauphas et al. (2002) report differences between IAB and IIICD irons, our data reveal the groups to have a common Mo isotope composition, which is indistinguishable from terrestrial Mo. Our results thus support the previously proposed concept of a genetic link between the groups, with a IAB/IIICD complex consisting of a main group and several subgroups (Wasson and Kallemeyn, 2002). A recent investigation of the IAB/IIICD complex furthermore found that while the sLL and sLM subgroups are isotopically consistent with the main group, the sHH and sHL subgroups have distinct Mo isotope compositions (Worsham and Walker, 2015). Our data provide support for the first of these statements, as all of the meteorites from the main group and sLL and sLM subgroups that were analysed here exhibit consistent Mo isotope data. However, since the reportedly anomalous sHH and sHL subgroups were not sampled for this study, no additional evidence is available for the latter observation.

It is also well documented that the neighbouring elements Mo and Ru have correlated s-process deficits (e.g., Dauphas et al., 2004; Fischer-Gödde et al., 2015). Using the Ru data of Chen et al. (2010) and the Mo data from this study, a linear regression of ε^{100}Ru vs. $\varepsilon^{92}Mo_{(8/6)}$ yields a slope of -0.44 ± 0.06 (Fig. 2). This result is in agreement with the predicted slope of -0.44, as calculated from the s-process abundances of Mo and Ru for SiC grains (Dauphas et al., 2004). Furthermore, Burkhardt et al. (2011) obtained a slope of -0.46 ± 0.06 for irons, main group pallasites, and ordinary and CV chondrites, when plotting the same Ru data with their own ε^{92}Mo results. A similar but slightly less precise slope of -0.51 ± 0.15 is obtained when $\varepsilon^{92}Mo_{(8/6)}$ is combined with the more recent Ru isotope data of Fischer-Gödde et al. (2015) (see Supplementary Material). Therefore, our new Mo results concur with the previously reported correlation of Ru and Mo isotopes in iron meteorites.

Previous work also posited that mass-independent Mo isotope anomalies can arise in iron meteorites as a result of exposure to galactic cosmic rays (Worsham et al., 2015), and/or nuclear volume field shifts (Fujii et al., 2006). Detailed examinations of these processes, as documented in the Supplementary Material, demonstrate that such effects will have no or only minimal impact on the Mo isotope compositions determined in this study. In addition, positive $\varepsilon^{97}Mo_{(8/6)}$ anomalies may, in principle, arise from radioactive decay of extinct ^{97}Tc ($t_{1/2} \sim 3.8$ Myr) to ^{97}Mo. However,

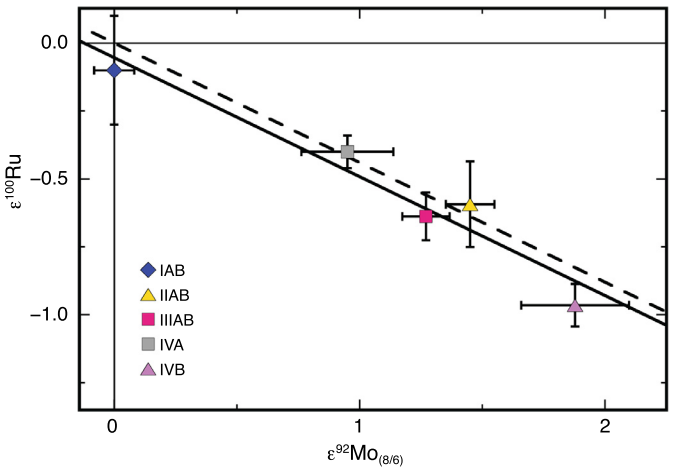

Fig. 2. Plot of ε^{100}Ru vs. ε^{92}Mo$_{(8/6)}$, showing the correlation of Mo and Ru nucleosynthetic isotope anomalies for iron meteorites. The Mo data are from this study, normalised to ^{98}Mo/^{96}Mo = 1.453174; the Ru data from Chen et al. (2010), normalised to ^{99}Ru/^{101}Ru = 0.7450754. All uncertainties are 2se of the group means. Regression of the data yields a slope of -0.46 ± 0.06 (black line), symptomatic for a correlation of s-process Mo and Ru isotopes, as calculated by Dauphas et al. (2004) (dashed line, slope = -0.44).

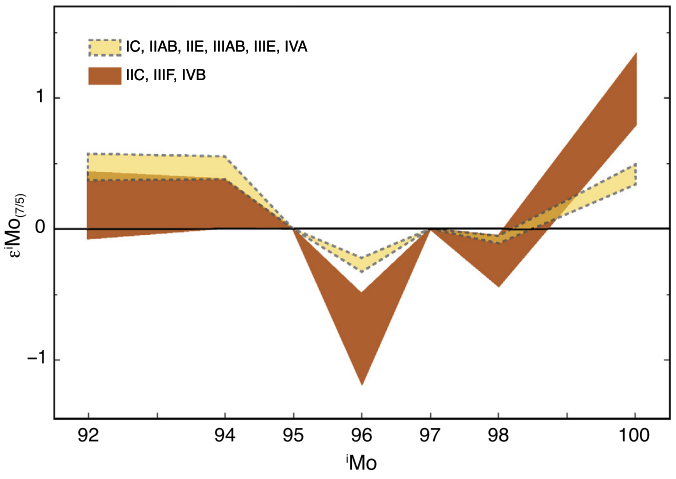

Fig. 3. Plot of iron meteorite data, normalised to ^{97}Mo/^{95}Mo, showing how the iron meteorite groups diverge into two suites. In one suite (shaded yellow), ε^{92}Mo$_{(7/5)} \approx \varepsilon^{100}Mo_{(7/5)}$, which corresponds to a 'pure' s-process deficit pattern (Fig. 1d). In the other suite (shaded brown), ε^{100}Mo$_{(7/5)} \gg \varepsilon^{92}Mo_{(7/5)}$. The yellow area shows the mean (±2se) of the IC, IIAB, IIE, IIIAB, IIIE and IVA groups. The brown area shows the mean (±2se) of the IIC, IIIF and IVB groups. (For interpretation of the references to colour in this figure legend, the reader is referred to the web version of this article.)

Dauphas et al. (2002) and Burkhardt et al. (2011) showed that any such contributions are also likely to be insignificant.

4.2. Molybdenum heterogeneity of the solar nebula

While the measured Mo isotope compositions closely approximate the s-process deficit models of Fig. 1, the data do not fit the predictions perfectly – there are minor but significant discrepancies. This is most noticeable for the ^{97}Mo/^{95}Mo normalisation: while the IICs have the highest ε^{100}Mo$_{(7/5)}$ values, they do not have the highest ε^{92}Mo$_{(7/5)}$, as would be expected if the patterns of all groups are dominated by pure s-process deficits. Instead, groups IC, IIAB, IIE, IIIAB, IIIE and IVA have higher ε^{92}Mo$_{(7/5)}$ than groups IIC, IIIF and IVB, and the opposite is true for ε^{100}Mo$_{(7/5)}$ (Fig. 3).

Since ^{97}Mo and ^{95}Mo have similar s- and r-process contributions (of 59% and 55%, respectively, for the s-process), the ^{97}Mo/^{95}Mo ratio is not significantly affected by s-deficits. Therefore, the discrepancies seen at ε^{92}Mo$_{(7/5)}$ and ε^{100}Mo$_{(7/5)}$ (Fig. 3) indicate variations in p- and r-process components – the IIC, IIIF and IVB groups display excesses in r-process relative to p-process components, whilst also showing excess overall abundances of p- and r-nuclides relative to s-process isotopes.

These effects are further assessed in three-isotope plots of ε^{i}Mo vs. ε^{i}Mo (Fig. 4). Also shown in these plots are lines representing mixing of terrestrial material with a p-process component, an r-process component and a component with an s-process deficit (orange, purple and green lines, respectively). Of particular significance is that diagrams involving p-, s- and r-process nuclides in either the plotted ε^{i}Mo values or the normalising ratio – for example, ε^{100}Mo$_{(7/5)}$ vs. ε^{92}Mo$_{(7/5)}$ (Fig. 4a) and ε^{96}Mo$_{(7/5)}$ vs. ε^{94}Mo$_{(7/5)}$ (Fig. 4b) – indicate the iron meteorite groups fall into the same two distinct suites. In these diagrams, groups IIC, IIIF and IVB plot between the s-deficit and r-excess mixing lines, whereas the IC, IIAB, IIE, IIIAB, IIIE and IVA groups plot around the s-deficit mixing lines. Crucially, where the ε^{i}Mo vs. ε^{i}Mo diagrams involve only s- and r-process isotopes, no such distinction is observed (Fig. 4c–d). Here, all groups from both suites plot around the s-deficit mixing lines, which are equivalent to r-excess lines, as the mixing involves only two components, s- and r-process nuclides. This provides further evidence that variations in p- and/or r-process components create the two suites, and the observed nucleosynthetic anomalies in groups IIC, IIIF and IVB are not a consequence of pure s-deficits. For simplicity, the pure s-deficit suite of iron meteorites (groups IC, IIAB, IIE, IIIAB, IIIE and IVA) is denoted as the *r=p suite* in the following, while the second suite with an excess of r- relative to p-process nuclides (IIC, IIIF and IVB), is denoted as the *r>p suite*.

The same offset from pure s-process deficits, and the separation into the two suites, is also found for results obtained with normalisation to ^{98}Mo/^{96}Mo (Fig. 5). In this case, however, the two suites are less well resolved because the s-process contributions to ^{98}Mo and ^{96}Mo differ more (at 76% and 100%, respectively) than for the ^{97}Mo–^{95}Mo couple. As a result, the s-deficit and r-excess mixing lines of Fig. 5 are closer together in ε^{i}Mo vs. ε^{i}Mo space and the compositions of the two suites are less distinct.

Significantly, it appears the Mo isotope differences between the suites cannot be explained by variations in s-process nucleosynthesis. Different models of s-process production are used to calculate the mixing lines of Fig. 4 and Fig. 5 (Arlandini et al., 1999; Bisterzo et al., 2011, 2014). These models take into account different sensitivities to branching during stellar evolution and associated uncertainties (e.g., the ^{13}C(α, n) and ^{22}Ne(α, n) reactions), yet they produce only a small range of Mo isotope compositions and the associated s-deficit mixing lines plot close together in Fig. 4 and Fig. 5. In plots that incorporate p-, s-, and r-process isotopes such that the divergence into two suites is apparent (i.e., Fig. 4a–b and Fig. 5a), the *r=p suite* overlaps with the different s-process mixing trends whilst the *r>p suite* plots well away. This indicates that variations in s-process contributions, which arise from different stellar evolutions, are unlikely to be responsible for the observed diversity of Mo isotope compositions.

Our observation of divergence into two suites is in accord with similar dichotomy observed between meteorite groups for Cr, Ni and Ti isotope anomalies (e.g., Steele et al., 2012; Warren, 2011). Moreover, our data are in excellent agreement with the suggestion of Budde et al. (2016) that two distinct Mo isotope reservoirs coexisted in the early solar nebula. These workers argue that the Mo isotope compositions of bulk carbonaceous chondrites, iron meteorites groups IID, IIIF, IVB, the Eagle Station pallasite, and the Tafassasset achondrite record an overall s-process deficit but also

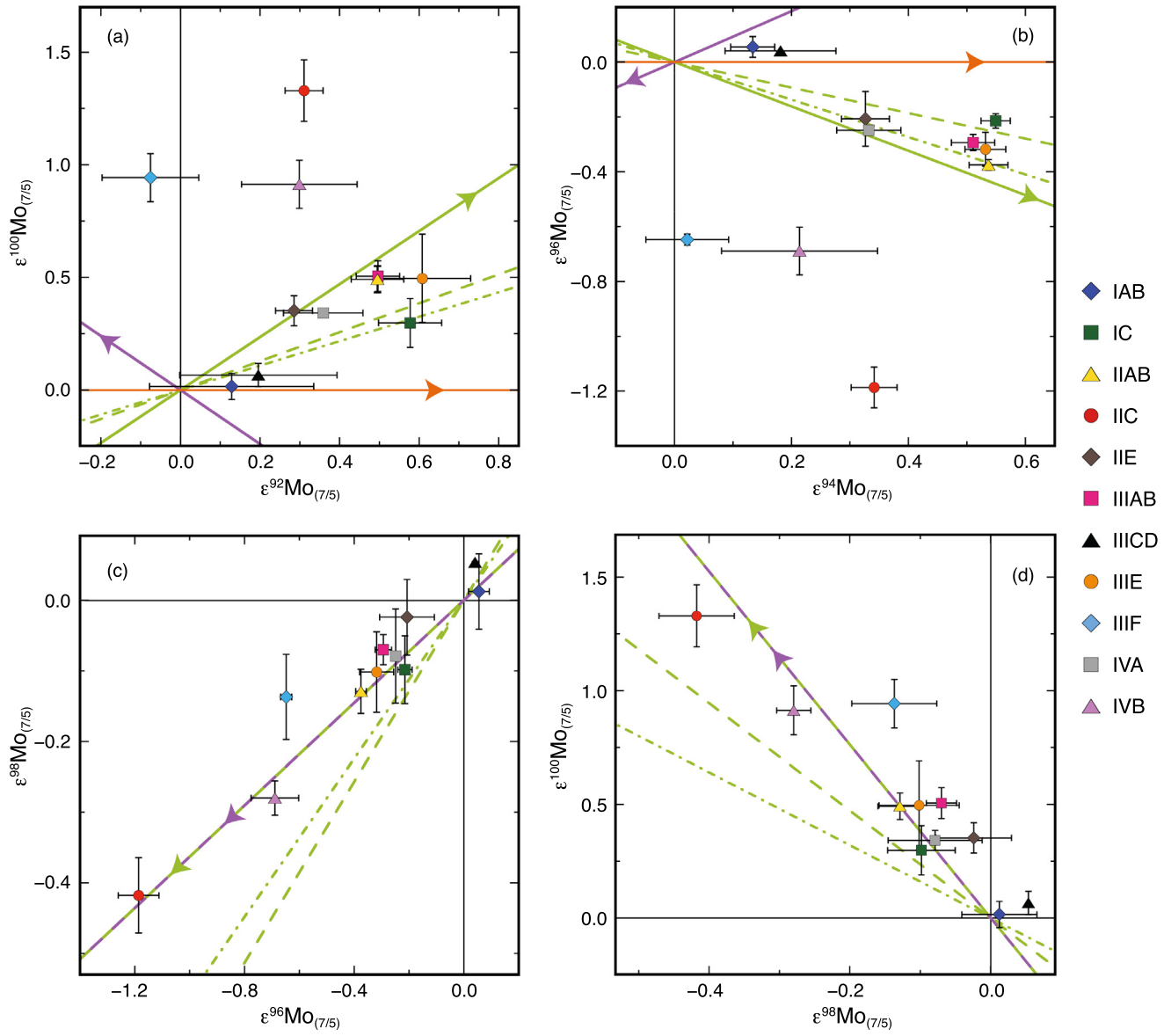

Fig. 4. Plots of ε^{i}Mo vs. ε^{i}Mo, normalised to ^{97}Mo/^{95}Mo, for iron meteorite data. Shown are group means with 2se uncertainties. Theoretical p-excess, r-excess and s-deficit mixing lines (orange, purple and solid green lines, respectively), calculated using the nucleosynthetic s-process production model of Arlandini et al. (1999), are also shown. For comparison, s-deficit mixing lines using the models of Bisterzo et al. (2011) (dashed green line) and Bisterzo et al. (2014) (dotted–dashed green line) are shown in addition. In (a) and (b), the data fall into two suites: the *r=p suite* of groups IC, IIAB, IIE, IIIAB, IIIE and IVA plots around the s-deficit mixing lines, whilst the *r>p suite* of groups IIC, IIIF and IVB plots between the r-excess and s-deficit mixing lines. In (c) and (d), the separate suites are not discernible as only s- and r-process isotopes are involved in the diagrams. (For interpretation of the references to colour in this figure legend, the reader is referred to the web version of this article.)

require the presence of an additional r-process component, which they suggest may be CAI-like material. They furthermore posit that enstatite and ordinary chondrites, angrites, main group pallasites and iron meteorite groups IAB, IIAB, IIE, IIIAB, IIICD, IIIE and IVA are in accord with a variable pure s-process deficit with no involvement of additional material. Integration of published chondrite data with our new iron meteorite results reveals similar groupings (Fig. 6). A best-fit line for the ordinary and enstatite chondrites and our *r=p suite* (solid line) is thereby distinct from the best-fit line for carbonaceous chondrites and *r>p suite* iron meteorites (dashed line). These groupings, referred to as *carbonaceous* and *non-carbonaceous meteorites* by Budde et al. (2016), are suggestive of genetic links between the particular chondrite and iron meteorite groups.

The more precise Mo isotope data of this study enable the two distinct iron meteorite groupings to be resolved with more confidence than was previously possible (see Supplementary Material). In addition, the results indicate that the Mo isotope compositions of iron meteorites (and, by inference chondrites) do not solely reflect a deficit of s-process nuclides relative to the Earth, but also record uncorrelated excesses in p- and r-process components.

4.3. Origin of isotopic heterogeneity

Our current understanding of solar system formation posits large-scale mixing and transport of material in the solar nebula, which entails, over time, the progressive homogenisation of isotopically diverse components. While the solar system is well mixed relative to the large intrinsic anomalies seen at the grain-size level (e.g., presolar grains in primitive meteorites), the existence of small but significant planetary-wide isotope anomalies (of about 10 to 100 ppm) for Mo and other elements shows the solar nebula was not completely homogenised at the time of parent body formation. A number of scenarios have been proposed to explain the origin

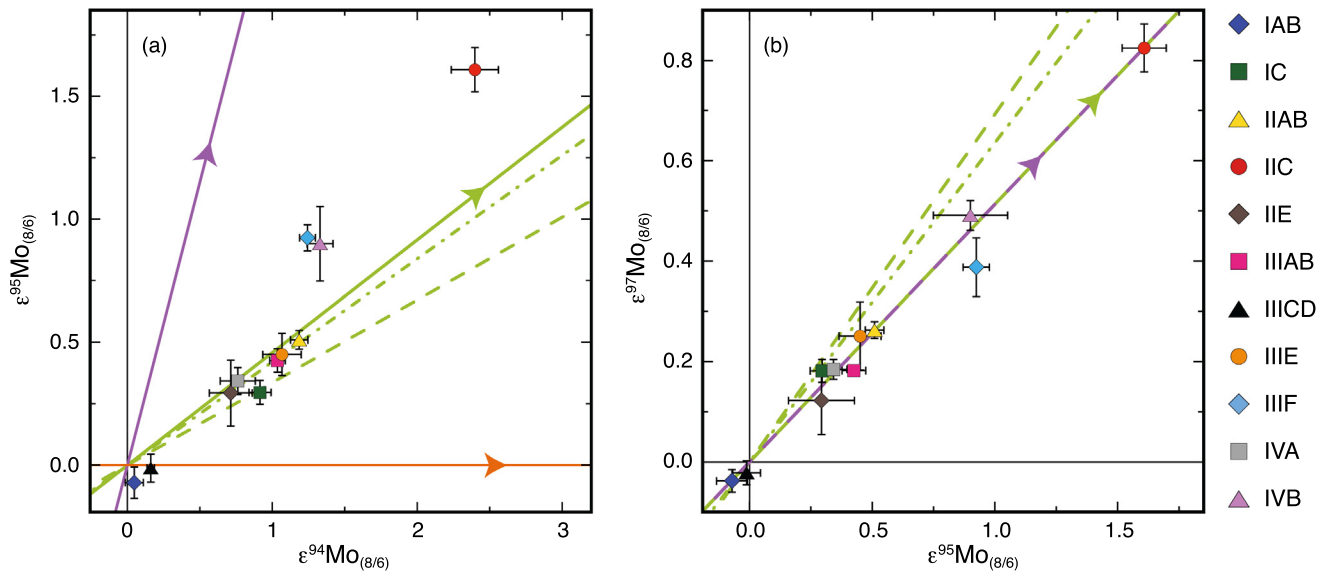

Fig. 5. Plots of ε^{i}Mo vs. ε^{i}Mo, normalised to ^{98}Mo/^{96}Mo, for iron meteorite data. Shown are group means with 2se uncertainties. Theoretical p-excess, r-excess and s-deficit mixing lines (orange, purple and solid green lines, respectively), calculated using the nucleosynthetic s-process production model of Arlandini et al. (1999), are also shown. For comparison, s-deficit mixing lines using the models of Bisterzo et al. (2011) (dashed green line) and Bisterzo et al. (2014) (dotted–dashed green line) are shown in addition. In (a) the data fall into two suites: the *r=p suite* of groups IC, IIAB, IIE, IIIAB, IIIE and IVA plot around the s-deficit mixing lines, while the *r>p suite* of groups IIC, IIIF and IVB plots in between the r-excess and s-deficit lines. In (b) the separate suites are not discernible as only s- and r-process isotopes are involved in the diagram. (For interpretation of the references to colour in this figure legend, the reader is referred to the web version of this article.)

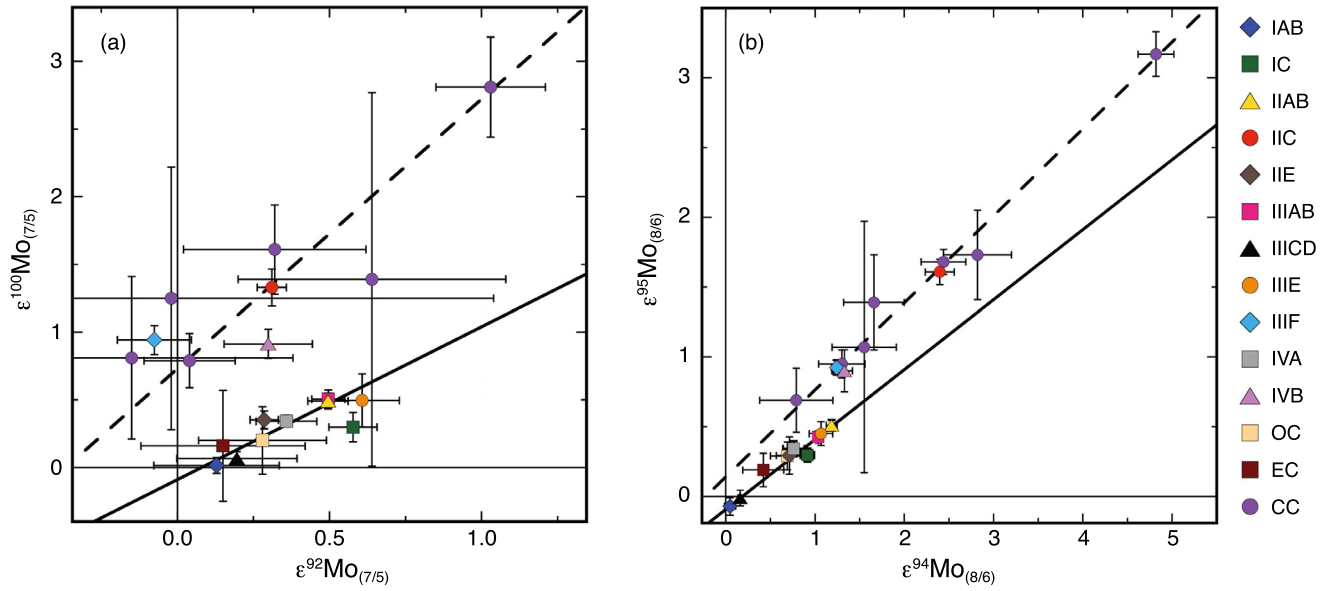

Fig. 6. Plots of ε^{i}Mo vs. ε^{i}Mo for iron meteorite and literature chondrite data. (a) $\varepsilon^{100}Mo_{(7/5)}$ vs. $\varepsilon^{92}Mo_{(7/5)}$, normalised to ^{97}Mo/^{95}Mo. (b) $\varepsilon^{95}Mo_{(8/6)}$ vs. $\varepsilon^{94}Mo_{(8/6)}$, normalised to ^{98}Mo/^{96}Mo. Iron meteorite data are group means with 2se uncertainties from this study. Chondrite data from Burkhardt et al. (2011), except for CK and CO (Burkhardt et al., 2014). Note that data for CK chondrites are not included in (a) as the uncertainties are too large. In both (a) and (b) the best-fit line for ordinary chondrites, enstatite chondrites and the *r=p suite* (solid line) is clearly distinct from the best-fit line for carbonaceous chondrites and the *r>p suite* (dashed line).

of these isotopic heterogeneities and the correlated or distinct behaviour that is exhibited by various elements.

The traditional explanation for the presence of nucleosynthetic isotope anomalies in bulk meteorites calls for a "cosmic chemical memory", in which heterogeneities still pertained at the time of parent body formation because the homogenisation of the nebula was not yet complete (Clayton, 1982; Dauphas et al., 2002). Some studies, however, developed an alternative model, whereby the solar nebula was initially homogeneous but received a late injection of isotopically anomalous material to impart heterogeneity during the period when early solids formed (e.g., Qin et al., 2011; Trinquier et al., 2007). Such a late injection of s-process rich material can, in principle, account for the Mo isotope anomalies observed here in iron meteorites and could also explain why the IAB/IIICD complex has a Mo isotope composition identical to Earth. The IAB/IIICD meteorites have relatively young ages in comparison to other irons (Markowski et al., 2006), giving the injected material more time to homogenise prior to parent body accretion. Late injection, however, cannot account for the Mo isotope compositions of chondrites, which accreted later than the IAB/IIICD irons but exhibit larger anomalies, sometimes even larger than the early accreted irons (Burkhardt et al., 2011). A further significant obstacle to the late injection model is provided by the bulk-rock Zr isotope data of Akram et al. (2015), which indicate heterogeneous distribution of different s-process phases derived from multiple stellar sources. These workers demonstrate that this is unlikely to

be a consequence of late injection of material from multiple stellar sources as the solar system is rather well mixed to a first order.

Consequently, it is becoming increasingly apparent that an alternative mechanism is required to explain the isotopic heterogeneity observed for many different elements and isotope systems. A consensus is thereby starting to develop, with more localised processes, either in the solar nebula or on parent bodies, being responsible for the isotopic anomalies of bulk meteorites.

One such model is the physical sorting of different dust grain types, which carry distinct isotopic signatures. Regelous et al. (2008) argue that Ni isotope anomalies reflect physical sorting of different phases (silicates, sulphides and metals) within the solar nebula. Subsequent localised and preferential removal or enrichment of distinct phases will thus produce isotopic variations in the remaining material, from which the meteorite parent bodies formed. Similarly, grain-size sorting has been posited as a mechanism for selectively excluding or enriching certain host phases, to create distinct isotope compositions in the solar nebula (Dauphas et al., 2010). However, the relationships between the isotope effects observed for Mo, Zr, Ti and Cr call this model into question. It was demonstrated that s-process deficits in Mo isotopes correlate with those reported for Zr (Akram et al., 2015). Furthermore, ^{96}Zr excesses in bulk meteorites vary proportionately with excesses in the neutron-rich isotope ^{50}Ti, which in turn correlate with excesses in ^{54}Cr (Schönbächler et al., 2011; Trinquier et al., 2009). It has been suggested that the anomalies in ^{54}Cr are caused by the heterogeneous distribution of nm-sized spinels from grain-size sorting in strong stellar winds during solar system formation (Dauphas et al., 2010). However, such spinels are low in Ti and hence cannot be responsible for the ^{50}Ti excesses (Qin et al., 2011). Given that the stellar winds, which may have sorted spinels, are very unlikely to have had the exact same interaction with the ^{50}Ti host phase(s), it appears unlikely that the isotope anomalies of Ti are generated by grain-size sorting (Akram et al., 2015). Therefore, an alternative mechanism is required to account for the observed relationship between the correlated Mo–Zr and Cr–Ti isotope anomalies.

Yokoyama et al. (2011) suggest aqueous alteration on parent bodies may have resulted in the selective modification and redistribution of isotopically anomalous presolar components. This explanation, however, also appears to be at odds with the correlated nature of the Mo and Zr isotope anomalies. Whilst Zr is an immobile element, Mo is sensitive to oxidation and readily interacts with fluids, thus allowing transport and redistribution (Akram et al., 2015). Alteration should hence result in a decoupling of Mo and Zr isotopes, yet this is not observed. Consequently, any alteration must have operated on a local scale only, without affecting bulk rock compositions, and therefore cannot be responsible for the Mo isotope anomalies observed in this study.

Increasingly, the most promising models for producing the observed isotopic variations in bulk meteorites invoke the destruction of thermally unstable presolar components in the nebula. For instance, Trinquier et al. (2009) report correlated mass-independent variations of ε^{46}Ti and ε^{50}Ti, even though these isotopes have different nucleosynthetic origins. They argue the correlation suggests the presolar dust inherited from the molecular cloud was well mixed when the earliest solids formed in the solar nebula. Subsequent thermal processing, however, resulted in the selective destruction of thermally unstable and isotopically anomalous components, thereby producing the planetary-scale isotopic variability observed in bulk meteorites.

A similar mechanism has been proposed to explain the decoupled Mo and W isotope compositions of bulk meteorites and their acid leachates (Burkhardt et al., 2012a, 2012b). Leachates of Murchison show broadly correlated Mo and W isotope anomalies associated with the variable distribution of s-process isotopes, and this demonstrates that anomalous Mo and W are hosted in the same carriers. However, such a correlation does not exist for bulk meteorites, as IIAB, IIIAB and IVA iron meteorites have W isotope compositions indistinguishable from the terrestrial value (after correction for radiogenic and cosmogenic effects), in contrast to the Mo isotope data presented here (e.g., Qin et al., 2008). Fundamental to the thermal processing model of Burkhardt et al. (2012b) is the observation that elements characterised by isotopic homogeneity (e.g., Hf, W, Os) are all highly refractory with 50% condensation temperatures of $Tc_{50} \approx 1700$–1800 K, whereas elements that display bulk-meteorite isotopic heterogeneities are slightly less refractory with somewhat lower condensation temperatures (e.g., $Tc_{50} = 1587$ K for Mo; Lodders, 2003). This can explain why the Mo and W isotope anomalies are decoupled at the bulk meteorite scale – under oxidising conditions Mo is much more volatile than W and is preferentially removed from the nebular dust by evaporation. This modifies the Mo isotope composition of the processed dust whilst W isotopes are largely unaffected.

However, such reasoning encounters difficulty with the observed Zr isotope heterogeneity. With a 50% condensation temperature of 1736 K, Zr is more refractory than Hf ($Tc_{50} = 1676$ K) and closely resembles W ($Tc_{50} = 1790$ K) (Lodders, 2003). Therefore, volatility cannot be the only factor that determines whether an element displays nucleosynthetic isotope anomalies from thermal processing. An alternative model proposes the most likely cause is the decoupling of 'light' ($Z \leq 56$) and 'heavy' ($Z > 56$) r-process nuclides (e.g., Akram et al., 2013; Wasserburg et al., 1996), which are believed to originate from different nucleosynthetic production sites. The heavy r-process isotopes are formed by the main r-process, with the preferred stellar site of neutron star mergers (Tsujimoto and Shigeyama, 2014). Conversely, the light r-process isotopes are thought to be produced predominantly by the weak r-process and charged particle reactions (CPRs) in Type II supernovae and their neutrino driven winds (Wanajo, 2013), with only small contributions from the main r-process.

Most elements with observed s- or r-process isotope heterogeneity in bulk meteorites have $Z \leq 56$ (Mo, Ba, Ca, Cr, Ni, Ru, Ti and Zr), whilst those with homogeneous isotope compositions feature $Z > 56$ (Hf, Os, Pt). However, recent studies of Nd ($Z = 60$) isotopes in meteorites revealed s-deficit anomalies, which correlate with those of Mo (Burkhardt et al., 2016; Render et al., 2017). While further investigations are desirable, the Nd data casts significant doubt on models proposing that light and heavy r-process isotopes have distinct isotopic signatures due to different production sites. In this context, it is noteworthy that some W ($Z = 74$) isotope studies reported small deficits of ^{184}W for IVB irons (e.g., Qin et al., 2008), although these anomalies of ~10 ppm are barely resolvable and several other investigations were unable to identify W isotope anomalies in bulk meteorites (e.g., Kleine et al., 2004).

As a consequence of these discrepancies, no single model is currently able to account for the numerous isotopic observations and explain why particular elements host nucleosynthetic isotope anomalies in bulk meteorites whilst others do not. Hence, it is likely that the nucleosynthetic isotope signatures are determined by a number of factors, including the mineralogy of the carrier phases, the distinct physical and chemical properties of the elements, and the timing and location at which the elements were affected by processes, such as grain sorting or heating and evaporation, in the early solar nebula (e.g., Burkhardt et al., 2016).

4.4. Updated thermal processing model based on Mo isotopes

In the context of thermal processing models, the s-process Mo isotope deficits observed for iron meteorites in this study are produced by the thermal destruction of unstable phases, which host r- and p-process nuclides. In the following, a modified thermal

processing model is presented, which specifically accounts for the observation of uncorrelated p- and r-process Mo isotope anomalies. In particular, the data reveal that iron meteorites of the *r=p suite* are characterised by 'pure' s-process deficits (i.e., correlated p- and r-excesses) coupled with relatively small s-deficits, in comparison to the terrestrial composition. In contrast, parent bodies of the *r>p suite* exhibit larger s-process deficits (relative to Earth) coupled with uncorrelated p- and r-excesses. The two suites are located in the '*r=p region*' and '*r>p region*', respectively, and the position of these regions in relation to the Sun is important due to the different thermal susceptibilities of the r- and p-process host phases. These regions can be considered equivalent to the *non-carbonaceous* and *carbonaceous* reservoirs identified by Budde et al. (2016). Those authors argue that meteorites of both reservoirs exhibit overall deficits in s-process nuclides, but only the *carbonaceous* reservoir (*r>p region*) features an additional excess of r-process material, which is superimposed on the s-deficits. Given the constraints posed by various other elements, it is reasonable to conclude that this excess of r-process component, as well as the overall s-deficits, arise from thermal processing of solar nebula material. Further details of the model and its justification are outlined below.

The solar nebula was initially isotopically homogeneous, as supported by the homogeneity observed for elements such as Hf and Os. Subsequent thermal processing of solar nebula dust then preferentially vaporised and removed Mo present in p- and r-process host phases, and the gas was separated from the dust prior to complete re-condensation. This could occur, for instance, when supernovae ejecta with highly anomalous p- and r-process material were first deposited as coatings on pre-existing grains in the interstellar medium (ISM) and then subsequently lost during re-heating (e.g., Dauphas et al., 2010). As a consequence, the residual dust, which accreted to form meteorite parent bodies and planets, had a relative excess of s-process isotopes and the extent of this excess is expected to vary with radial distance from the Sun. Material from the inner solar system experienced more heating and evaporation, due to the proximity of the Sun, and should thus have a greater proportion of s-process isotopes in comparison to dust that was processed in the cooler outer regions of the solar nebula.

In the context of this model, the new Mo isotope data suggest that the IIC parent body formed furthest from the Sun, whilst the IAB/IIICD parent body accreted close to the Earth, with other iron meteorite parent bodies forming at intermediate distances. This inference is further supported by published Mo data for chondrites (Burkhardt et al., 2014, 2011). These workers observed larger deficits of s-process Mo isotopes for carbonaceous chondrites than for ordinary and enstatite chondrites (Fig. 6), in agreement with the well-supported conclusion that the parent bodies of the former meteorites accreted at a greater distance from the Sun than the latter (Chambers, 2006). Furthermore, enstatite chondrites are thought to have formed closer to the Sun than ordinary chondrites (Chambers, 2006), in accord with the observation that the former have more Earth-like Mo isotope compositions (with smaller s-deficits) than ordinary chondrites.

Significantly, independent findings also suggest that the divergence of the iron meteorite data into two suites, as a result of abundance variations in p- vs. r-process Mo isotopes, is in accord with thermal processing of early solar system material. Whilst p- and r-process Mo isotopes are both thought to form during explosive nucleosynthesis, they are not expected to originate entirely from the same stellar sites. In detail, p-process Mo is thought to form in both Type Ia and Type II supernovae, while the r-process isotopes are primarily produced by the weak r-process and CPRs in Type II supernovae (e.g., Travaglio et al., 2011; Wanajo, 2013). Phases that formed in Type II supernovae, which host both p- and r-process Mo, are therefore expected to have very similar susceptibilities to thermal processing, but the p-process components from Type Ia supernovae likely have distinct properties.

Meteorite parent bodies of the *r=p suite* have 'pure' s-process deficits, which indicates that the r- and p- process host phases had similar susceptibilities to thermal processing in the relatively hot *r=p region* close to the Sun. At greater heliocentric distances in the *r>p region*, the thermal processing of dust was less intense, as revealed by larger s-process deficits relative to the terrestrial composition. The literature chondrite data provide further support for this interpretation. In particular, the observation that carbonaceous chondrites cluster with the *r>p suite* of irons whilst the ordinary and enstatite chondrites group with the *r=p suite* (Fig. 6) concurs with the conclusion that the former meteorites formed at a greater distance from the Sun than the latter (Chambers, 2006).

In addition to the overall s-deficits, iron meteorites of the *r>p suite* display an excess of r-process components relative to p-process isotopes. This suggests that p-process host phases were more susceptible to thermal processing than the r-process carriers in the cooler *r>p region*. Such an observation is in line with the prediction that Type Ia supernova dust is more fine-grained than the ejecta of Type II supernovae (Meyer and Clayton, 2015; Yu et al., 2013). At greater heliocentric distances, where thermal processing is reduced, the smaller grain size of Type Ia supernova dust may thus have resulted in preferential evaporation and loss of p-process isotopes, producing the uncorrelated p- and r-excesses (relative to Earth) seen in the *r>p region*.

In summary, the updated thermal processing model is able to successfully relate both the variable deficits of s-process Mo isotopes and effects observed between r- and p-process components with the extent of thermal processing, and thereby with heliocentric distance.

5. Conclusions

New Mo isotope analyses of iron meteorites were carried out and these cover the broadest range of samples studied to date, with results that show improved precision in comparison to previous investigations. The results provide clear evidence for variable planetary-scale deficits in s-process nuclides, which indicate that the solar nebula was not isotopically homogeneous at the time of iron meteorite parent body formation. Analyses of the previously unstudied IIC group reveal the most anomalous Mo isotope compositions yet determined for irons, suggesting that it may be fruitful to explore further rare and ungrouped samples. Conversely, non-magmatic IAB/IIICD complex iron meteorites display terrestrial Mo isotope compositions, with all other irons showing intermediate values.

The improved precision afforded by this study enabled the identification of two isotopically distinct suites of iron meteorites. The *r=p suite*, which includes groups IC, IIAB, IIE, IIIAB, IIIE and IVA, exhibits only small deficits in s-process isotopes relative to the Earth, coupled with 'pure' s-deficits due to correlated excesses of p- and r-process components. In contrast, the *r>p suite*, encompassing groups IIC, IIIF and IVB, displays larger overall s-process deficits relative to the terrestrial composition, coupled with excesses in r-process relative to p-process components.

Comparison of the new Mo data with results for other elements (Ba, Cr, Hf, Nd, Ni, Os, Ru, Ti, W, Zr) suggests the most likely cause of the Mo isotope variability is thermal processing of material in the solar nebula, with associated selective destruction of unstable presolar phases. An updated model is presented for this process, in which both the magnitude of the s-process Mo isotope deficits and the correlated vs. uncorrelated nature of r- and p-process isotope abundances are determined by the extent of thermal processing and governed primarily by heliocentric distance. The *r=p suite* of

iron meteorite parent bodies formed closer to the Sun (and hence in proximity to the Earth), thereby experiencing strong thermal processing to exhibit small s-process deficits relative to the terrestrial composition. In contrast, the *r>p suite* formed in the cooler outer solar nebula, where more subtle thermal processing removed a smaller proportion of p- and r-process host phases, generating larger s-process deficits relative to the Earth. In addition, the less intense temperatures enabled selective destruction of p- versus r-process carrier phases, producing the observed uncorrelated abundances of r- and p-process Mo isotopes.

Acknowledgements

We wish to thank N. Dauphas and a second reviewer for their constructive and thorough reviews, and C. Sotin for editorial efforts. The MAGIC group, and Katharina Kreissig in particular, is thanked for helping to keep the mass spec running and the clean labs organised. Deborah Cassey and Natasha Almeida are thanked for their help in selecting appropriate specimens from the NHM meteorite collection. Jane Barling and Alex Halliday from Oxford helpfully supplied copious quantities of a NIST SRM 3134 Mo solution for the analyses, while Tim Elliott (Bristol) sportingly sourced us some NIST SRM 361. Discussion of early manuscript drafts with Maria Schönbächler and Tina van de Flierdt supported substantive improvements of the interpretations. The project was supported by a research grant from STFC to MR (ST/J001260/1), an STFC studentship to GP, and a NERC Fellowship to TG (NE/G01499X/2).

Appendix A. Supplementary material

Supplementary material related to this article can be found online at http://dx.doi.org/10.1016/j.epsl.2017.05.001.

References

Akram, W., Schönbächler, M., Bisterzo, S., Gallino, R., 2015. Zirconium isotope evidence for the heterogeneous distribution of s-process materials in the solar system. Geochim. Cosmochim. Acta 165, 484–500.

Akram, W., Schönbächler, M., Sprung, P., Vogel, N., 2013. Zirconium–hafnium isotope evidence from meteorites for the decoupled synthesis of light and heavy neutron-rich nuclei. Astrophys. J. 777, 169–180.

Arlandini, C., Kappeler, F., Wisshak, K., Gallino, R., Lugaro, M., Busso, M., Straniero, O., 1999. Neutron capture in low-mass asymptotic giant branch stars: cross sections and abundance signatures. Astrophys. J. 525, 886–900.

Bisterzo, S., Gallino, R., Straniero, O., Cristallo, S., Kappeler, F., 2011. The s-process in low-metallicity stars, II: interpretation of high-resolution spectroscopic observations with asymptotic giant branch models. Mon. Not. R. Astron. Soc. 418, 284–319.

Bisterzo, S., Travaglio, C., Gallino, R., Wiescher, M., Kappeler, F., 2014. Galactic chemical evolution and solar s-process abundances: dependence on the C-13-pocket structure. Astrophys. J. 787, 10.

Budde, G., Burkhardt, C., Brennecka, G.A., Fischer-Gödde, M., Kruijer, T.S., Kleine, T., 2016. Molybdenum isotopic evidence for the origin of chondrules and a distinct genetic heritage of carbonaceous and non-carbonaceous meteorites. Earth Planet. Sci. Lett. 454, 293–303.

Burkhardt, C., Borg, L.E., Brennecka, G.A., Shollenberger, Q.R., Dauphas, N., Kleine, T., 2016. A nucleosynthetic origin for the Earth's anomalous Nd-142 composition. Nature 537, 394–398.

Burkhardt, C., Hin, R.C., Kleine, T., Bourdon, B., 2014. Evidence for Mo isotope fractionation in the solar nebula and during planetary differentiation. Earth Planet. Sci. Lett. 391, 201–211.

Burkhardt, C., Kleine, T., Dauphas, N., Wieler, R., 2012a. Nucleosynthetic tungsten isotope anomalies in acid leachates of the Murchison chondrite: implications for hafnium–tungsten chronometry. Astrophys. J. Lett. 753, L6.

Burkhardt, C., Kleine, T., Dauphas, N., Wieler, R., 2012b. Origin of isotopic heterogeneity in the solar nebula by thermal processing and mixing of nebular dust. Earth Planet. Sci. Lett. 357, 298–307.

Burkhardt, C., Kleine, T., Oberli, F., Pack, A., Bourdon, B., Wieler, R., 2011. Molybdenum isotope anomalies in meteorites: constraints on solar nebula evolution and origin of the Earth. Earth Planet. Sci. Lett. 312, 390–400.

Chambers, J.E., 2006. Meteoritic diversity and planetesimal formation. In: Lauretta, D.S., McSween Jr., H.Y. (Eds.), Meteorites and the Early Solar System II. University of Arizona Press, Tuscon, Arizona, pp. 487–497.

Chen, J.H., Papanastassiou, D.A., Wasserburg, G.J., 2010. Ruthenium endemic isotope effects in chondrites and differentiated meteorites. Geochim. Cosmochim. Acta 74, 3851–3862.

Clayton, D.D., 1982. Cosmic chemical memory – a new astronomy. Q. J. R. Astron. Soc. 23, 174–212.

Dauphas, N., Davis, A.M., Marty, B., Reisberg, L., 2004. The cosmic molybdenum–ruthenium isotope correlation. Earth Planet. Sci. Lett. 226, 465–475.

Dauphas, N., Marty, B., Reisberg, L., 2002. Molybdenum evidence for inherited planetary scale isotope heterogeneity of the protosolar nebula. Astrophys. J. 565, 640–644.

Dauphas, N., Remusat, L., Chen, J.H., Roskosz, M., Papanastassiou, D.A., Stodolna, J., Guan, Y., Ma, C., Eiler, J.M., 2010. Neutron-rich chromium isotope anomalies in supernova nanoparticles. Astrophys. J. 720, 1577–1591.

Dauphas, N., Schauble, E.A., 2016. Mass fractionation laws, mass-independent effects, and isotopic anomalies. Annu. Rev. Earth Planet. Sci. 44 (44), 709–783.

Fischer-Gödde, M., Burkhardt, C., Kruijer, T.S., Kleine, T., 2015. Ru isotope heterogeneity in the solar protoplanetary disk. Geochim. Cosmochim. Acta 168, 151–171.

Fisker, J.L., Hoffman, R.D., Pruet, J., 2009. On the origin of the lightest molybdenum isotopes. Astrophys. J. Lett. 690, L135–L139.

Fujii, T., Moynier, F., Telouk, P., Albarede, F., 2006. Mass-independent isotope fractionation of molybdenum and ruthenium and the origin of isotopic anomalies in Murchison. Astrophys. J. 647, 1506–1516.

Kleine, T., Mezger, K., Munker, C., Palme, H., Bischoff, A., 2004. Hf-182-W-182 isotope systematics of chondrites, eucrites, and martian meteorites: chronology of core formation and early mantle differentiation in Vesta and Mars. Geochim. Cosmochim. Acta 68, 2935–2946.

Lodders, K., 2003. Solar system abundances and condensation temperatures of the elements. Astrophys. J. 591, 1220–1247.

Lu, Q., Masuda, A., 1994. The isotopic composition and atomic-weight of molybdenum. Int. J. Mass Spectrom. Ion Process. 130, 65–72.

Markowski, A., Quitte, G., Halliday, A.N., Kleine, T., 2006. Tungsten isotopic compositions of iron meteorites: chronological constraints vs. cosmogenic effects. Earth Planet. Sci. Lett. 242, 1–15.

Meyer, B.S., Clayton, D.D., 2015. Sizes of carbon grains condensing in SNII shells. In: 78th Annual Meeting of the Meteoritical Society, #5318.

Qian, Y.Z., Wasserburg, G.J., 2007. Where, oh where has the r-process gone? Phys. Rep. 442, 237–268.

Qin, L., Dauphas, N., Wadhwa, M., Markowski, A., Gallino, R., Janney, P.E., Bouman, C., 2008. Tungsten nuclear anomalies in planetesimal cores. Astrophys. J. 674, 1234–1241.

Qin, L., Nittler, L.R., Alexander, C.M.O., Wang, J., Stadermann, F.J., Carlson, R.W., 2011. Extreme Cr-54-rich nano-oxides in the CI chondrite Orgueil – implication for a late supernova injection into the solar system. Geochim. Cosmochim. Acta 75, 629–644.

Regelous, M., Elliott, T., Coath, C.D., 2008. Nickel isotope heterogeneity in the early Solar System. Earth Planet. Sci. Lett. 272, 330–338.

Render, J., Fischer-Gödde, M., Burkhardt, C., Kleine, T., 2017. The cosmic molybdenum–neodymium isotope correlation and the building material of the Earth. Geochem. Perspect. Lett. 3, 170–178.

Schiller, M., Paton, C., Bizzarro, M., 2015. Evidence for nucleosynthetic enrichment of the protosolar molecular cloud core by multiple supernova events. Geochim. Cosmochim. Acta 149, 88–102.

Schönbächler, M., Akram, W.M., Williams, N.H., Leya, I., 2011. Nucleosynthetic heterogeneities of neutron-rich isotopes in calcium aluminium-rich inclusions and bulk solar system materials. In: Formation of the First Solids in the Solar System, #9085.

Steele, R.C.J., Coath, C.D., Regelous, M., Russell, S., Elliott, T., 2012. Neutron-poor nickel isotope anomalies in meteorites. Astrophys. J. 758, 59.

Travaglio, C., Gallino, R., Rauscher, T., Roepke, F.K., Hillebrandt, W., 2015. Testing the role of SNe Ia for Galactic chemical evolution of p-nuclei with 2D models and with s-process seeds at different metallicities. Astrophys. J. 799, 54.

Travaglio, C., Ropke, F., Gallino, R., Hillebrandt, W., 2011. Type Ia supernovae as sites of the p-process: two-dimensional models coupled to nucleosynthesis. Astrophys. J. 739, 93.

Trinquier, A., Birck, J.L., Allegre, C.J., 2007. Widespread Cr-54 heterogeneity in the inner solar system. Astrophys. J. 655, 1179–1185.

Trinquier, A., Elliott, T., Ulfbeck, D., Coath, C., Krot, A.N., Bizzarro, M., 2009. Origin of nucleosynthetic isotope heterogeneity in the solar protoplanetary disk. Science 324, 374–376.

Tsujimoto, T., Shigeyama, T., 2014. Enrichment history of r-process elements shaped by a merger of neutron star pairs. Astron. Astrophys. 565, L5.

Wanajo, S., 2013. The r-process in proto-neutron-star wind revisited. Astrophys. J. Lett. 770, L22.

Wanajo, S., Janka, H.T., Kubono, S., 2011. Uncertainties in the vp-process: supernova dynamics versus nuclear physics. Astrophys. J. 729, L46.

Warren, P.H., 2011. Stable-isotopic anomalies and the accretionary assemblage of the Earth and Mars: a subordinate role for carbonaceous chondrites. Earth Planet. Sci. Lett. 311, 93–100.

Wasserburg, G.J., Busso, M., Gallino, R., 1996. Abundances of actinides and short-lived nonactinides in the interstellar medium: diverse supernova sources for the r-processes. Astrophys. J. 466, L109–L113.

Wasson, J.T., Kallemeyn, G.W., 2002. The IAB iron–meteorite complex: a group, five subgroups, numerous grouplets, closely related, mainly formed by crystal segregation in rapidly cooling melts. Geochim. Cosmochim. Acta 66, 2445–2473.

Worsham, E.A., Bermingham, K.R., Walker, R., 2015. Cosmic ray exposure modification of the molybdenum isotopic composition of iron meteorites. In: AGU Fall Meeting, #65206.

Worsham, E.A., Walker, R.J., 2015. Molybdenum isotope evidence for diverse genetics among IAB iron meteorite complex subgroups. In: 46th Lunar and Planetary Science Conference, #2524.

Yokoyama, T., Alexander, C.M.O., Walker, R.J., 2011. Assessment of nebular versus parent body processes on presolar components present in chondrites: evidence from osmium isotopes. Earth Planet. Sci. Lett. 305, 115–123.

Yokoyama, T., Walker, R.J., 2016. Nucleosynthetic isotope variations of siderophile and chalcophile elements in the Solar System. Rev. Mineral. Geochem. 81, 107–160.

Yu, T.H., Meyer, B.S., Clayton, D.D., 2013. Dust growth in core-collapse and thermonuclear supernovae. In: 76th Annual Meeting of the Meteoritical Society, #5328.

Zinner, E., 2007. Presolar grains. In: Holland, H.D., Turekian, K.K. (Eds.), Treatise on Geochemistry. Pergamon, Oxford, pp. 1–33.